

# Study of ion cyclotron range of frequencies heating characteristics in deuterium plasma in the Large Helical Device

journal or publication title	Nuclear Fusion
volume	62
number	1
page range	016004
year	2021-12-02
NAIS	12951
URL	<a href="http://hdl.handle.net/10655/00013113">http://hdl.handle.net/10655/00013113</a>

doi: <https://doi.org/10.1088/1741-4326/ac359d>



PAPER • OPEN ACCESS

# Study of ion cyclotron range of frequencies heating characteristics in deuterium plasma in the Large Helical Device


To cite this article: S. Kamio *et al* 2022 *Nucl. Fusion* **62** 016004

View the [article online](#) for updates and enhancements.

You may also like

- [The geometry of the ICRF-induced wave-SOL interaction. A multi-machine experimental review in view of the ITER operation](#)  
L. Colas, G. Urbanczyk, M. Goniche et al.
- [Effects of ICRF power on SOL density profiles and LH coupling during simultaneous LH and ICRF operation on Alcator C-Mod](#)  
C Lau, Y Lin, G Wallace et al.
- [Optimization of ICRH for core impurity control in JET-ILW](#)  
E. Lerche, M. Goniche, P. Jacquet et al.

# Study of ion cyclotron range of frequencies heating characteristics in deuterium plasma in the Large Helical Device

S. Kamio<sup>1,\*</sup> , K. Saito<sup>1,2</sup>, R. Seki<sup>1,2</sup>, H. Kasahara<sup>1</sup>, M. Kanda<sup>1</sup>, G. Nomura<sup>1</sup> and T. Seki<sup>1</sup>

<sup>1</sup> National Institute for Fusion Science, National Institutes of Natural Sciences, Toki, 509-5292, Japan

<sup>2</sup> The Graduate University for Advanced Studies, SOKENDAI, Toki, Gifu, 509-5292, Japan

E-mail: [kamio@nifs.ac.jp](mailto:kamio@nifs.ac.jp)

Received 23 June 2021, revised 5 October 2021

Accepted for publication 2 November 2021

Published 2 December 2021



CrossMark

## Abstract

The characteristics of ion cyclotron range of frequencies (ICRF) minority ion heating with a hydrogen minority and deuterium majority plasma were studied by ICRF modulation injection experiments in the Large Helical Device (LHD). In recent experiments with deuterium plasma, no significant increase in the neutron emission rate due to ICRF second harmonic deuteron heating was observed. Therefore, in this study, the neutron emission rate was used to refer to the information regarding the thermal ion component. Like the results of the observations of the heating efficiencies at various minority proton ratios, the experimental results showed good agreement with the simple model simulation of ICRF wave absorption. During these experiments, the accelerated minority hydrogen ions were observed by neutral particle analyzers. The counting rates of the energetic particles were higher in the lines of sight passing through the helical ripple than across the magnetic axis, and the counting rate decreased as the minority hydrogen ion ratio increased. The dependence of the minority hydrogen ion ratio on the density of the energetic ions was consistent with the experimentally observed heating efficiencies and simulations. The heating efficiency of ICRF minority ion heating could be well explained by simple model simulation in the LHD deuterium experiment.

Keywords: ICRF, minority ion heating, power modulation, LHD

(Some figures may appear in colour only in the online journal)

## 1. Introduction

In ion cyclotron range of frequencies (ICRF) heating, the ions which satisfy resonance conditions are mainly accelerated by the wave and fast ions are produced. The bulk electrons and ions are heated directly by the wave and/or indirectly via the fast ions. Because an ICRF wave can produce

energetic particles up to MeVs or higher, and can heat the central electrons, new ICRF heating experiments are planned in W7-X [1] and ITER [2]. In experiments in the Joint European Torus (JET) with an ITER-like wall [3, 4], the properties of a plasma heated with an ICRF wave were investigated for use in ITER. The heating efficiencies were evaluated by break-in-slope (BIS) analysis for minority hydrogen ion heating in a deuterium plasma. For huge devices, ICRF minority ion heating is expected to be useful for initial phase heating with low plasma parameters and for wall conditioning instead of large-scale baking.

It is known that the heating efficiency of minority ion heating strongly depends on the minority ion ratio. However, in

\* Author to whom any correspondence should be addressed.



Original content from this work may be used under the terms of the [Creative Commons Attribution 4.0 licence](https://creativecommons.org/licenses/by/4.0/). Any further distribution of this work must maintain attribution to the author(s) and the title of the work, journal citation and DOI.

an experiment for steady-state operation of the Large Helical Device (LHD) [5–8], the minority ion ratio spontaneously changed during the discharge due to the outgas from the wall or the divertor tiles. Therefore, it is important to clarify the heating efficiency of ICRF minority ion heating with respect to the minority ion ratio, not only for optimization of the heating system in future device designs but also for control of wall discharge cleaning. In order to investigate the effect of ICRF injection, plasma confinement and relaxation also need to be understood. Therefore, a comprehensive understanding of ICRF heating characteristics is useful for new experiments using ICRF heating. In the LHD, the ICRF heating characteristics can be investigated by ICRF power modulation experiments using multiple measurements. Power modulation experiments are often used for analysis of the heat transport process in experimental fusion research [9, 10]. During ICRF power modulation experiments, the plasma parameters, such as ion and electron temperatures, are changed according to the ICRF power modulation. During the experiments we assume a certain steady-state plasma, but on the other hand we cannot analyze the effect of power modulation unless we can measure the change in the plasma during power modulation. Therefore, we set the modulation amplitude to less than 10% of the total injection power. Because ICRF power modulation can be easily modeled, this method is effective for a comprehensive understanding of ICRF heating characteristics.

The ICRF heating characteristics have been studied in the LHD for many years in hydrogen or helium plasmas [11, 12] using flexible and high power injection and many diagnostics. In the LHD, ICRF minority ion heating with minority hydrogen and majority helium is the main heating method, for example in steady-state operation or for wall discharge cleaning [13], because the heating efficiency is higher than with second or higher harmonic heating [14–16]. The ICRF wave accelerates the minority hydrogen and the ion temperature increases due to relaxation of the energetic particles. The efficiency of ICRF minority ion heating depends on the minority ion ratio, the plasma density, the ion and electron temperatures and other conditions. Among these parameters, the minority ion ratio is one of the most controllable aspects for increasing the heating efficiency. For example, in steady-state operation, the electron density and the total injection power are required to be constant with the parameters maintained using the control system [17]. Therefore, the minority ion ratio should be adjusted so as not to decrease the absorbed power. From these perspectives, it is important to understand the dependence of the heating efficiency on the minority ion ratio. In previous studies, the ICRF minority hydrogen ion heating efficiency in dependence on the minority hydrogen ion ratio was obtained experimentally in a helium plasma [18, 19].

Since the 2019 financial year ICRF minority hydrogen ion heating experiments have been started in a deuterium majority plasma in the LHD. When the ICRF wave directly couples and accelerates the deuterons, the neutron emission rate should be clearly increased, as seen in the experiments in JET or ASDEX-U [20, 21], by ICRF third-harmonic heating with neutral beam (NB) injection. In the LHD, the experimentally observed neutron emission rate agreed with the calculation

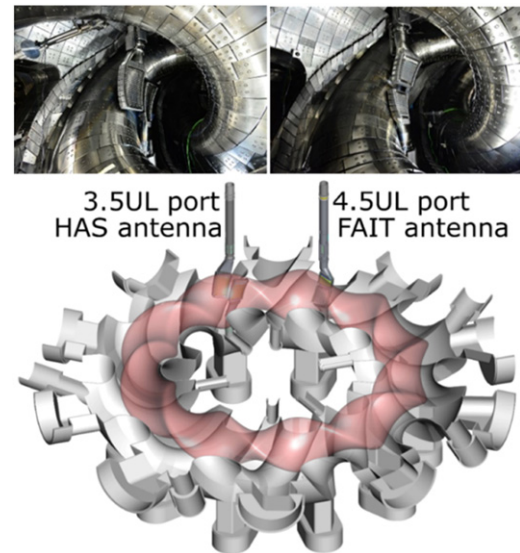


**Figure 1.** Schematic view of the LHD and photographs of the ICRF antennas inside the vacuum chamber.

using the thermal fusion reactivity of deuterium plasma [22]. In other words, information on the bulk deuterium ions can be understood through the neutron measurements. In this study, we analyzed the stored energy and fast ion measurements as well as the neutron emission rate, which varied in a complicated manner according to power modulation. The characteristics of ICRF minority hydrogen ion heating, especially for heating efficiencies including the ratio to bulk ions and electrons, were investigated in the LHD deuterium plasma.

## 2. Experimental setup

A schematic view of the LHD and photographs of the ICRF antennas in recent campaigns are shown in figure 1. The poloidal and toroidal period number  $l/m = 2/10$  the typical plasma minor radius  $a_p$  in a vacuum is 0.64 m when the major radius  $R_{ax} = 3.6$  m. In this study, two pairs of antennas are used, called the HAS antenna and FAIT antenna. They are located at 3.5 port and 4.5 port, respectively in the LHD's 10 toroidal sections. The antennas are installed from the upper and lower ports of the LHD vacuum chamber, and the antennas can move toward the plasma by changing the pivot degrees inside the vacuum chamber. As shown in figure 1, the HAS antenna is a toroidal array antenna and the FAIT antenna is a poloidal array antenna. By changing the phase of the antenna current in the upper and lower antennas, the HAS antenna can change  $k_{||}$ . The dipole phase is usually used because of its higher heating efficiency than the monopole phase. Both antennas are used for ICRF heating with a fixed frequency of 38.47 MHz. By optimization at the fixed frequency, the loading resistances are increased by increasing the impedance of the antenna using impedance transformers [23].

Figure 2 shows a poloidal cross-section view of the LHD together with the FAIT antenna, the plasma flux surfaces and the ICRF cutoff and resonance layers of a standard magnetic

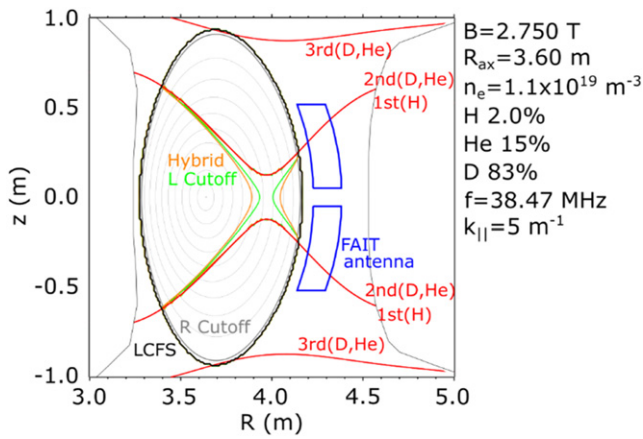


**Figure 2.** Poloidal cross-section view of the LHD with the ICRF antenna, the cutoff and the resonance layers of the ICRF wave in experimental conditions.

field configuration for  $B_t = 2.75$  T and  $R_{ax} = 3.60$  m. Typical experimental conditions are used for the calculation. The ICRF antennas are located at the outboard side of the plasma. We conducted ICRF injection experiments by changing the antenna position between 4.5 cm and 12 cm, but no significant difference was found in the heating efficiency. The typical distance between the plasma last closed flux surface (LCFS) and the antenna head is 7.0 cm for the FAIT antenna and 8.0 cm for the HAS antenna. For experiments without ICRF injection, the antennas stay at 12–14 cm from the LCFS.

### 3. Results and discussions

The ICRF heating efficiency can be estimated from the ICRF power modulation experiments. BIS analysis is often used to derive the ICRF heating efficiency [24]. On the other hand, by modulating the ICRF power rather than reducing the power altogether, the ICRF heating efficiency can be derived when the plasma is sustained. The modulation amplitude of the stored energy can be used to derive the heating efficiency by the following equations [25–27]:

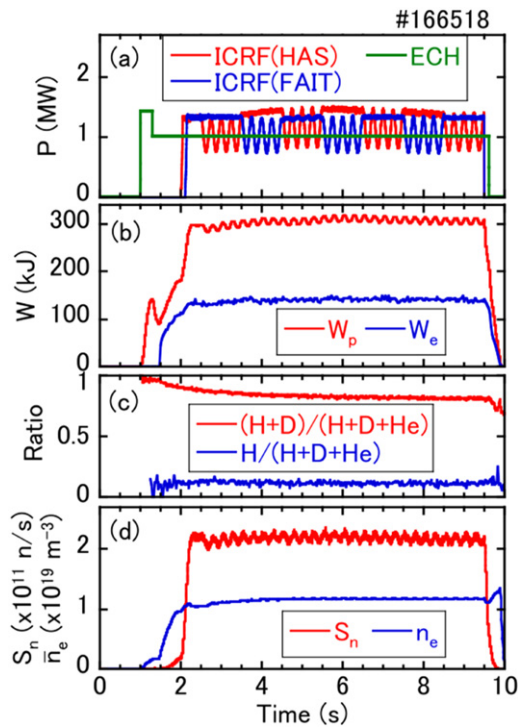
$$\frac{dW_p}{dt} = \eta P_{ICRF} - \frac{W_p}{\tau_E},$$

$$\eta = \frac{\omega}{\sin \delta_p} \frac{|\tilde{W}_p|}{|P_{ICRF}|},$$

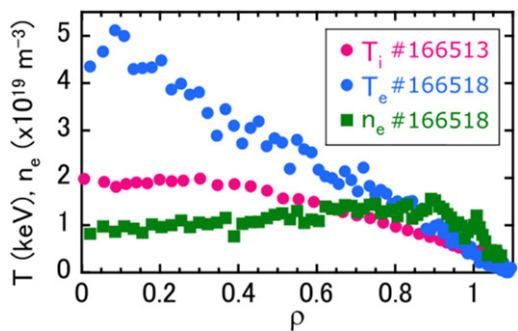
where  $W_p$  is the plasma stored energy,  $\eta$  is the ICRF heating efficiency,  $\tau_E$  is the plasma confinement time,  $\tilde{W}_p$  and  $\tilde{P}_{ICRF}$  indicate the amplitudes of  $W_p$  and  $P_{ICRF}$ ,  $\omega$  is the modulation frequency and  $\delta_p$  is the phase delay of the stored energy from the ICRF power modulation. Here, we evaluated  $\eta$  without dependence on the injection power  $P_{ICRF}$ . The evaluation of  $\eta$  including the dependence on the ion temperature or injection power was discussed in [27]. The measurement of the diamagnetic loops assumes energy isotropy in toroidal and poloidal directions. Therefore, if the ICRF wave accelerates the ions in the poloidal direction, these equations for obtaining  $\eta$  may cause overestimations.

Figure 3 shows a typical discharge in the ICRF power modulation injection experiment for evaluating heating efficiency. In this study, electron cyclotron heating (ECH) is also used to sustain the plasma, since there are many kinds of ICRF injection experiments superimposed on ECH, such as steady-state operation. As shown in figure 3(a), the ICRF power of the HAS and FAIT antennas is modulated separately to obtain the heating efficiency of each antenna. The time evolution of the electron stored energy  $W_e$  is also shown in figure 3(b), as measured by Thomson scattering. The ion species ratios are shown in figure 3(c). The ion ratios are estimated by using data from passive spectroscopy measurement [28]. Because the optical emissions  $H_\alpha$ ,  $D_\alpha$  and HeI are from low temperature neutrals, the measurement region for the intensity ratio is outside the plasma. Although the ion species ratio in the center may be different from that at the edge due to the isotope effect, we assumed that the ion ratios are the same inside and outside since it is difficult to measure the ratio at the center. In this study, we did not use pellet injection nor did we use the minimal NB injection to avoid inaccuracy in the ion ratios. Note that it is difficult to observe the exact low hydrogen or low deuterium ratios because the wavelengths of  $H_\alpha$  and  $D_\alpha$  are very close to each other. Figure 3(d) shows the time evolutions of the line-averaged electron density  $\bar{n}_e$  and the neutron emission rate  $S_n$ . The response to ICRF power modulation injection can also be seen clearly in  $S_n$ . The energy of the bulk ion is considered to be responding to the injection power. As in the experiment in the WEST device [29], which used ICRF minority hydrogen ion heating in deuterium plasma with similar plasma parameters to the experiment in the LHD, the neutron emission data were used to estimate the ion energy  $W_i$ . The spatial distributions of the temperature and density are shown in figure 4. The bulk ion temperature was measured by charge exchange spectroscopy (CXs) using perpendicular NB (p-NB) injection. The pulse of the p-NB was 5.0 ms, which is the minimum pulse length for measuring the ion temperatures in order not to affect  $W_p$ . Also, the ion temperature was measured in a different discharge to avoid coupling of the ICRF wave to p-NB particles during the modulation experiments. The electron density has a hollow profile. The electron density  $n_e$  and the temperatures  $T_e$  and  $T_i$  are approximately  $1.2 \times 10^{19} \text{ m}^{-3}$ , 2.8 keV, and 1.6 keV, respectively, at around  $\rho = 0.5$ .

A diamond neutral particle analyzer (DNPA) [30, 31] and a compact neutral particle analyzer (CNPA) [32] are used to observe the accelerated minority hydrogen ions. A NPA measures the energetic ions after charge exchange with neutral particles. Therefore, the count of observed energetic particles should be divided by  $\sigma v$  to consider the density of energetic ions inside the plasma. The analytic charge exchange cross sections are referred to the JAERI-Data/Code [33]. Figure 5(a) shows the lines of sight of the three spatial channels of the DNPA and figure 5(b) shows the line of sight of the CNPA. The lines of sight of DNPA channel 4 and the CNPA pass through the magnetic axis, and the lines of sight of DNPA channels 1 and 7 pass through the helical ripple where the energetic particles are considered to be trapped. Figure 5(c) shows the observed energy distributions of the accelerated ions in a similar discharge. The measurable energy region of the DNPA



**Figure 3.** Typical waveforms of the ICRF power modulation injection experiment. Time evolution of (a) injection powers, (b) stored energies, (c) ion ratios and (d) the neutron emission rate  $S_n$  and electron density  $n_e$  during the ICRF power modulation experiment.



**Figure 4.** Spatial distributions of the  $T_i$ ,  $T_e$  and  $n_e$ .  $T_i$  is observed by CXS in a similar discharge with short-pulse p-NB injection.

is from  $>40$  keV to some MeV, and the CNPA region is bulk energies of  $<150$  keV. The increase in the DNPA counts near 40 keV is considered to be due to thermal noise, because the DNPA detector is a semiconductor type detector. On the other hand, because the CNPA is an  $E||B$ -type NPA, the high counting rate at less than 20 keV can be considered to be a bulk component. The effective temperatures of each channels are shown in the figure. The line-averaged electron density of this discharge  $\bar{n}_e = 0.7 \times 10^{19} \text{ m}^{-3}$  is lower than the discharge shown in figure 3. The density of the energetic particles strongly depends on the electron density. Therefore, the lower electron density discharge is shown here to clearly see the difference in the energy distributions according to the measurement lines of sight. The results in figure 5(c) show that

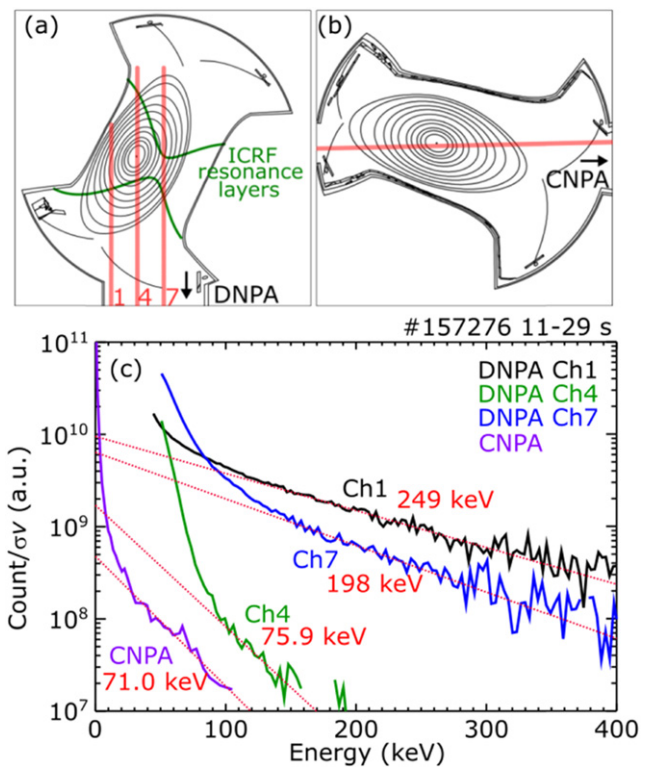


**Figure 5.** Lines of sight of (a) three DNPA channels and (b) the CNPA. (b) Energy distributions of the accelerated energetic particles observed by the NPAs.

the effective temperatures of DNPA channels 1 and 7 are higher than those of DNPA channel 4 and the CNPA. Even though the DNPA and CNPA have different detection methods, DNPA channel 4 and CNPA, which have similar lines of sight, observed similar effective temperatures. It is therefore confirmed in this experiment that the high counting rate of the energetic particles and high effective temperatures observed on the channels passing through the helical ripple indicate that the energetic particles accelerated by the ICRF wave are trapped in the helical ripple.

Figure 6 shows details of the modulation signals of (a)  $P_{\text{ICRF}}$ , (b)  $W_p$  and (c)  $S_n$  for the discharge shown in figure 3, and conditional averaged signals of (d)  $C/\sigma v$ , (e)  $W_e$  and (f)  $W_i$ . Here,  $C/\sigma v$  is the observed count for DNPA channel 1 divided by  $\sigma v$ . The amplitudes and phases of the 4 Hz modulation signals were estimated using the fast Fourier transform. The amplitudes of the signals of stored energies are  $|\bar{W}_p| = 13.4 \text{ kJ}$  and  $|\bar{W}_e| = 2.2 \text{ kJ}$ . The phase delays from  $P_{\text{ICRF}}$  are  $\delta_p = 39.6 \text{ ms}$ ,  $\delta_{S_n} = 52.0 \text{ ms}$ ,  $\delta_{C/\sigma v} = 16.8 \text{ ms}$  and  $\delta_e = 21.3 \text{ ms}$ . Here,  $\delta_{S_n}$  can be considered to be the phase delay of the stored energy of the bulk deuterons, since the significant increase in  $S_n$  due to direct deuteron heating is negligible under these experimental conditions [22]. On the other hand,  $\delta_{C/\sigma v}$  reflects the phase delay of the stored energy of the energetic particles. However, it is difficult to discuss details because the count of the NPA includes information on the neutral density as  $C/\sigma v = n_{\text{fast}} \times n_{\text{neutral}}$ . The phase delay of the NPA signals  $\delta_{C/\sigma v}$  should be considered carefully even though  $n_{\text{neutral}}$  seems to be constant during ICRF power modulation.

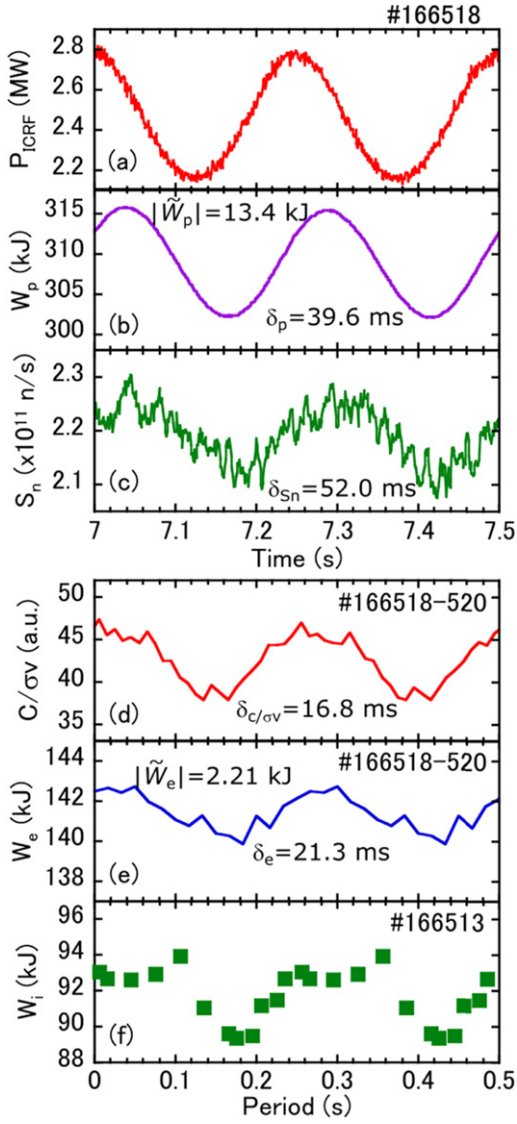


**Figure 6.** Time evolution of (a)  $P_{\text{ICRF}}$ , (b)  $W_p$  and (c)  $S_n$ , and conditional averaged signals of (d)  $C/\sigma v$  of DNPA channel 1, (e)  $W_e$  and (f)  $W_i$ .

Since we also observed fluctuation of the optical emissions of  $H_\alpha$ ,  $D_\alpha$  and He I, the neutral density could be slightly changed by modulation of the ICRF heating power. Therefore, it is difficult to estimate the phase delay of the minority hydrogen ions  $\tilde{W}_H$  from the observed phase delay of  $C/\sigma v$ .

Direct measurement of  $W_i$  by CXS of a similar discharge is shown in figure 6(f). The amplitude of  $W_i$  is calculated by assuming that  $Z_{\text{eff}} = 1$ . Therefore, it is difficult to discuss this using the amplitude of  $W_i$ . In both electron and ion measurement by Thomson scattering and CXS, the reaction of the spatial distributions of  $T_e$  or  $T_i$  to ICRF power modulation could not be observed because the amplitudes were similar to the noise level.

The experimental and simulation results of the heating efficiencies for various minority hydrogen ion ratios are shown in figure 7. The heating efficiencies of the HAS and FAIT antennas were observed separately using  $\tilde{W}_p$  for each modulation timing. The dashed lines are the results of the estimation

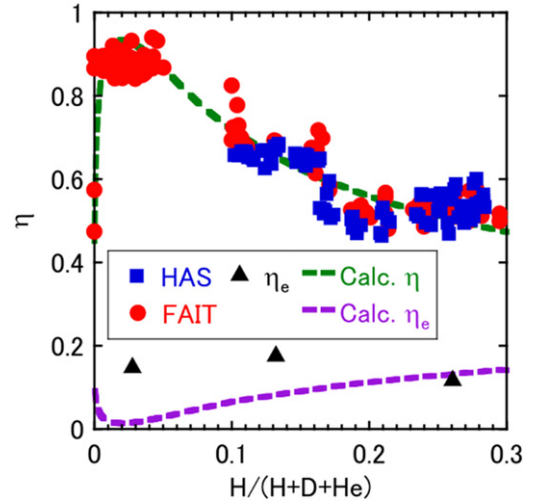


**Figure 7.** Experimental and simulation results for the heating efficiencies depending on the minority hydrogen ratio.

of the total heating efficiency and the efficiency of electron direct heating using a simple model simulation [18, 34]. In this simulation, the absorbed power  $P_{\text{abs}}/|E|^2$  was calculated assuming the condition of a constant electric field  $|E|$  in the region of possible propagation. The representative wave number  $k_{\parallel} = 5.0 \text{ m}^{-1}$  was used for the simulation. The heating efficiency can be written with the coefficients of absorption  $\alpha$  and loss of the electric field  $\beta$  as

$$\eta = \frac{P_{\text{abs}}}{P_{\text{ICRF}}} = \frac{\alpha|E|^2}{\alpha|E|^2 + \beta|E|^2}.$$

The ratio of the coefficients of loss and absorption of the electric field  $\beta/\alpha$  is held constant in the different minority hydrogen ion ratios because the frequency of the ICRF wave is fixed.  $\beta/\alpha$  is decided by fitting of the experimental results. Since the dependence of heating efficiency on the minority hydrogen ion ratio is similar in the experiment and the simulation shown in figure 7, the simulation results show good agreement with the experimental results. The dashed line for the heating efficiency of electrons  $\eta_e$  in figure 7 indicates the component of the direct heating of electrons by Landau damping or by electron transit-time magnetic pumping (TTMP). In order to estimate the electron heating component experimentally, we considered each component of the stored energies of  $W_H$ ,  $W_e$  and  $W_i$  as

$$\begin{aligned} \frac{dW_H}{dt} &= \eta_H P_{\text{ICRF}} - \frac{W_H}{\tau_{H-e}} - \frac{W_H}{\tau_{H-i}} - \frac{W_H}{\tau_H}, \\ \frac{dW_e}{dt} &= \eta_e P_{\text{ICRF}} + \frac{W_H}{\tau_{H-e}} + \frac{W_i}{\tau_{i-e}} - \frac{W_e}{\tau_{e-i}} - \frac{W_e}{\tau_e}, \\ \frac{dW_i}{dt} &= \frac{W_H}{\tau_{H-i}} + \frac{W_e}{\tau_{e-i}} - \frac{W_i}{\tau_{i-e}} - \frac{W_i}{\tau_i}, \end{aligned}$$

where  $\tau_H$ ,  $\tau_e$  and  $\tau_i$  are the confinement times of the minority hydrogen, the electrons and the bulk ions, respectively. Here, the component of the direct heating to bulk ions and energy relaxation from bulk plasma to minority ions are ignored. The

absorbed energies from the ICRF wave are mutually relaxing with energy slowing down times of  $\tau_{H-e}$ ,  $\tau_{H-i}$ ,  $\tau_{e-i}$  and  $\tau_{i-e}$ . In the evaluation of heating efficiency by modulation experiments, direct heating to the electrons and heating via minority hydrogen ions can be considered separately. In the equation for the electron stored energy, if we ignore the component of energy influx from energetic hydrogen ions  $W_H/\tau_{H-e}$  and from ions  $W_i/\tau_{i-e}$ , the following equation for evaluating the electron heating efficiency can be derived independently as

$$\eta_e = \frac{\omega}{\sin \delta_e} \frac{|\tilde{W}_e|}{|\tilde{P}_{ICRF}|}.$$

The absolute value of  $W_H/\tau_{H-e}$  is not clear. However,  $W_H/\tau_{H-e}$  is lower in high minority hydrogen ion ratios than low minority hydrogen ion ratios because  $W_H$  is lower in high minority hydrogen ion ratios than in low minority hydrogen ion ratios. The experimentally observed  $\eta_e$ , ignoring  $W_H/\tau_{H-e}$  and  $W_i/\tau_{i-e}$ , is shown by black triangles in figure 7. The simulation results for electron direct heating are not similar to the experimental results in the lower minority hydrogen ion region. In the lower hydrogen minority ion region, the component of electron direct heating is much lower than that of minority hydrogen ion heating.

The energy distributions of the energetic particles at various minority hydrogen ratios measured by DNPA channel 1 are shown in figure 8. Both the observed effective temperature and the total number of counts of the energetic minority hydrogen ions are higher in the lower minority hydrogen ion ratio discharges with the same electron density and temperature. One reason for this extension of the minority hydrogen ion tail in the lower minority hydrogen ion ratio is that the power density is higher for smaller numbers of minority hydrogen ions. Another reason is that the heating efficiency of minority hydrogen ion  $\eta_H$  is higher when the minority hydrogen ion ratio is low. By using the results for  $W_p$ ,  $W_e$  and  $W_i$ ,  $W_H$  can be estimated from

$$W_H = W_p - W_e - W_i.$$

$W_H$  is estimated as 79 kJ for a hydrogen ratio of 0.1, and 45 kJ when the hydrogen ratio is 0.3. The heating efficiencies for minority hydrogen  $\eta_H$  calculated in the simulation are 0.65 and 0.33 when the minority hydrogen ratios are 0.1 and 0.3, respectively. The simulation results are well reproduced, with the heating efficiency for minority hydrogen approximately halving when the minority hydrogen ratio goes from 0.1 to 0.3.

Figure 9 shows the phase delays of  $W_p$ ,  $S_n$  and  $W_e$ . When the minority hydrogen ion ratio is increased, the phase delays  $\delta_p$  decreased,  $\delta_e$  decreased and  $\delta_{S_n}$ , which is considered to be  $\delta_i$ , increased. Unfortunately, the phase delay  $\delta_H$  could not be evaluated from the experiments. The phase delays reflect a complex interplay of energy confinement times and energy relaxation times of each component. Since the electron density is constant under these experimental conditions, the energy confinement times and energy relaxation times are considered to be almost the same. Therefore, the differences in the delay

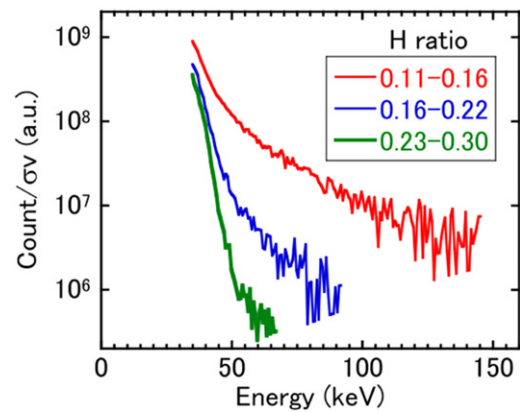


Figure 8. Energy distributions of the accelerated ions measured by DNPA channel 1.

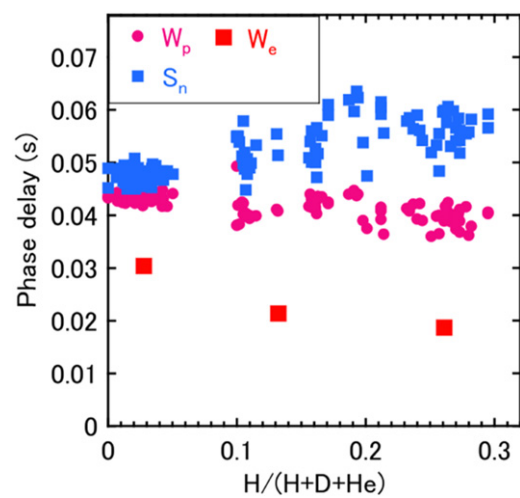
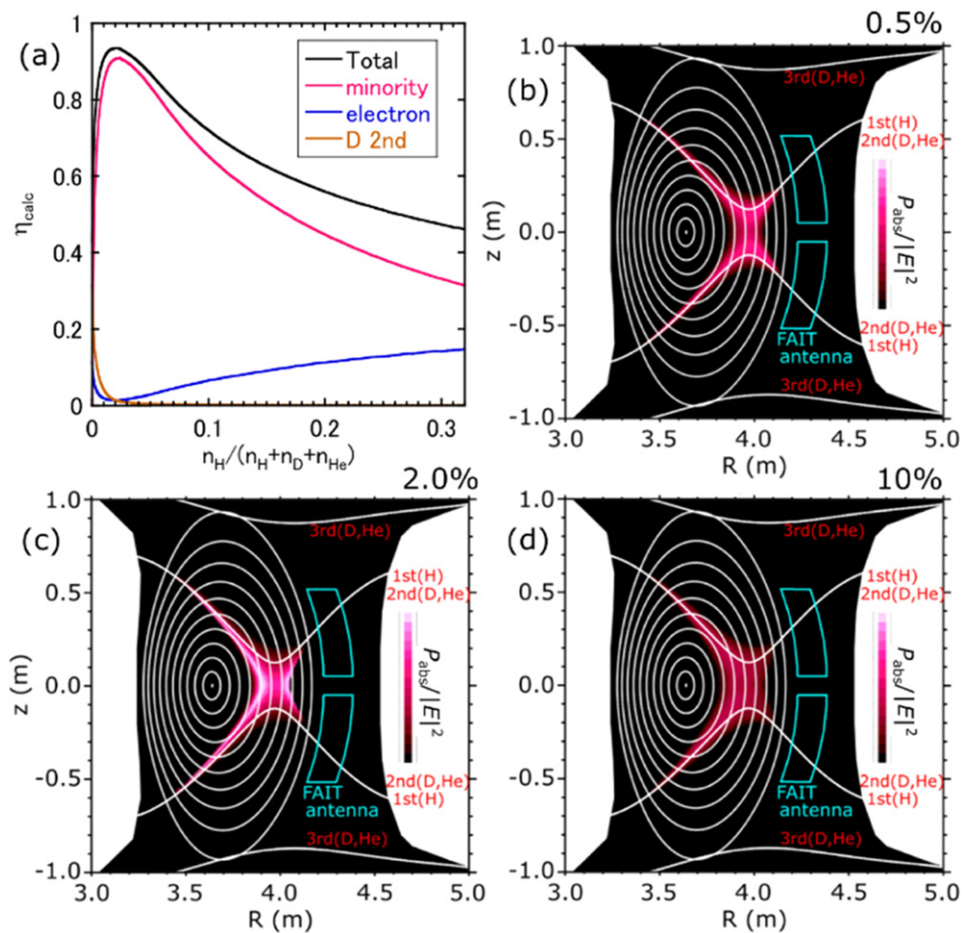


Figure 9. Phase delays of the modulation signal of  $W_p$ ,  $S_n$  and  $W_e$  from  $P_{ICRF}$ .

times are considered to be related to the ratio of the heating source. For example, the bulk electrons are heated by the ICRF wave directly or by energy relaxation of the accelerated minority hydrogen ions. The larger the percentage of direct heating, the shorter the delay, which is consistent with the experimental data for  $\delta_e$ . In any case, a detailed comparison with simulations needs to be done, which is a subject for future work.

The simulation results from the simple model simulation are shown in figure 10. Figure 10(a) shows the heating efficiencies of minority hydrogen by minority hydrogen ion heating, of electrons by Landau damping or by TTMP, of bulk deuterium by second harmonic heating and their total for various minority hydrogen ion ratios. According to the simulation results, the heating efficiency of bulk deuterium ion direct heating is less than 0.2 despite there being no minority hydrogen ion condition at this electron density. Therefore, in the region of this experimental condition the neutron emission rate is not increased significantly. For higher electron densities, the heating efficiency of bulk deuterium ion direct heating becomes higher. The results of the efficiencies of electrons and the total efficiency are also shown in figure 7 for comparison with the





**Figure 10.** (a) Heating efficiencies estimated by simple model calculations. (b)–(d) Spatial distributions of the absorbed power in the calculation for minority hydrogen ion ratios of (b) 0.5%, (c) 2.0% and (d) 10%.

experimental results. Figures 10(b)–(d) show the spatial distributions of the absorbed power. The absorbed powers are indicated by the different colors. The colors of the contour in figures 10(b)–(d) are normalized so that the effective absorption can be compared. At the highest efficiency, for the minority ratio of 2.0% shown in figure 10(c), strong absorption can be seen around the region where the left-hand polarized electric field is locally strong. The region with the highest absorption  $\rho = 0.5$  is local and mostly inside the region of absorption  $\rho = 0.4$ – $0.8$ . For higher minority hydrogen ratios, as shown in figure 10(d), the ICRF wave is absorbed in a wider area.

#### 4. Conclusion

The characteristics of ICRF minority hydrogen heating in the LHD deuterium plasma were studied. The neutron emission rate is considered to be the result of the fusion reaction of thermal deuterons. In order to estimate the heating efficiency, an ICRF power modulation experiment was performed. During ICRF power modulation, the responses were observed not only to the stored energy  $W_p$  but also the neutron emission rate

$S_n$ , the counting rate of the NPAs  $C/\sigma v$ , the electron stored energy  $W_e$  and the ion stored energy  $W_i$ . The observed heating efficiencies for various minority hydrogen ion ratios showed good agreement with the results of the simple model simulation. The ICRF wave was absorbed at around  $\rho = 0.4$ – $0.8$ , and in the case of a minority hydrogen ion ratio of approximately 2.0% strong absorption is expected around  $\rho = 0.5$ . The ICRF injection power modulation experiments with many kinds of diagnostics revealed that the wave absorption for minority hydrogen heating in the deuterium plasma was well explained by simple model simulation. The energetic minority hydrogen ions are observed to have a high effective temperature in the experiments with a low minority hydrogen ion ratio. It was confirmed that a high counting rate of energetic particles and high effective temperatures were observed on the NPA channels passing through the helical ripple, indicating that the energetic particles accelerated by the ICRF wave are trapped in the helical ripple. For high minority hydrogen ion ratios, the observed counts of the energetic minority hydrogen ions decreased, and the electron heating efficiency by Landau damping or TTMP,  $\eta_e$ , was in agreement with the simple model calculation.

## Acknowledgments

The authors wish to thank the LHD experiment group for their excellent support of this work.

## ORCID iDs

S. Kamio  <https://orcid.org/0000-0003-0755-2433>

## References

- [1] Ongena J. et al 2014 *Phys. Plasmas* **21** 061514
- [2] Lamalle P. et al 2015 *AIP Conf. Proc.* **1689** 030007
- [3] Jacquet P. et al 2014 *AIP Conf. Proc.* **1580** 65
- [4] Lerche E. et al 2014 *Nucl. Fusion* **54** 073006
- [5] Kasahara H. et al 2014 *Phys. Plasmas* **21** 061505
- [6] Saito K. et al 2005 *J. Nucl. Mater.* **337–339** 995–9
- [7] Tokitani M. et al 2015 *J. Nucl. Mater.* **463** 91–8
- [8] Motojima G. et al 2015 *J. Nucl. Mater.* **463** 1080–3
- [9] Luce T.C. et al 1994 *Plasma Phys. Control. Nucl. Fusion Res.* **1** 319
- [10] O'Rourke J. et al 1992 *Nucl. Fusion* **32** 1861
- [11] Kumazawa R. et al 2003 *Plasma Phys. Control. Fusion* **45** 1037–50
- [12] Mutoh T. et al 2013 *Nucl. Fusion* **53** 063017
- [13] Takahashi H. et al 2015 *J. Nucl. Mater.* **463** 1100–03
- [14] Kasahara H. et al 2006 *J. Korean Phys. Soc.* **49** S192–6
- [15] Saito K., Seki T., Kumazawa R., Kasahara H., Shimpo F., Nomura G. and Mutoh T. 2010 *Plasma Fusion Res.* **5** S1030
- [16] Kamio S., Seki R., Seki T., Saito K., Kasahara H., Sakakibara S., Nomura G. and Mutoh T. 2018 *Nucl. Fusion* **58** 126004
- [17] Kamio S., Kasahara H., Seki T., Saito K., Seki R., Nomura G. and Mutoh T. 2015 *Fusion Eng. Des.* **101** 226–30
- [18] Saito K. et al 2001 *Nucl. Fusion* **41** 1021–35
- [19] Saito K. et al 2010 *Fusion Sci. Technol.* **58** 515–23
- [20] Hellesen C. et al 2010 *Nucl. Fusion* **50** 022001
- [21] Tardini G. et al (The ASDEX Upgrade Team) 2012 *J. Inst.* **7** C03004
- [22] Seki R. et al 2020 *Plasma Fusion Res.* **15** 1202088
- [23] Saito K., Seki T., Kasahara H., Seki R., Kamio S., Nomura G. and Mutoh T. 2017 *J. Phys.: Conf. Ser.* **823** 012007
- [24] Gambier D.J. et al 1990 *Nucl. Fusion* **30** 23
- [25] Shoji T. et al 1986 *IPPJ* **18** 795 (<https://www.ipen.br/biblioteca/rel/R48851.pdf>)
- [26] Lerche E.A. and van Eester D. 2008 *Plasma Phys. Control. Fusion* **50** 035003
- [27] Torii Y. et al 2001 *Plasma Phys. Control. Fusion* **43** 1191–210
- [28] Morita S., Goto M., Masuzaki S. and Ashikawa N. (LHD Experimental Group) 2008 *Plasma Fusion Res.* **3** S1037
- [29] Colas L. et al 2020 *AIP Conf. Proc.* **2254** 040004
- [30] Kamio S., Fujiwara Y., Ogawa K., Isobe M., Seki R., Nuga H., Nishitani T. and Osakabe M. (The LHD Experiment Group) 2019 *J. Inst.* **14** C08002
- [31] Kamio S. et al 2020 *Rev. Sci. Instrum.* **91** 113304
- [32] Ozaki T. et al 2006 *AIP Conf. Proc.* **812** 399
- [33] Ito R. et al 1994 *JAERI-Data/Code* 94-005 ([https://inis.iaea.org/search/search.aspx?orig\\_q=RN:26013469](https://inis.iaea.org/search/search.aspx?orig_q=RN:26013469))
- [34] Saito K., Seki R., Kamio S., Kasahara H. and Seki T. 2020 *Plasma Fusion Res.* **15** 2402015